

Highly Stable Skyrmion State in Helimagnetic MnSi Nanowires

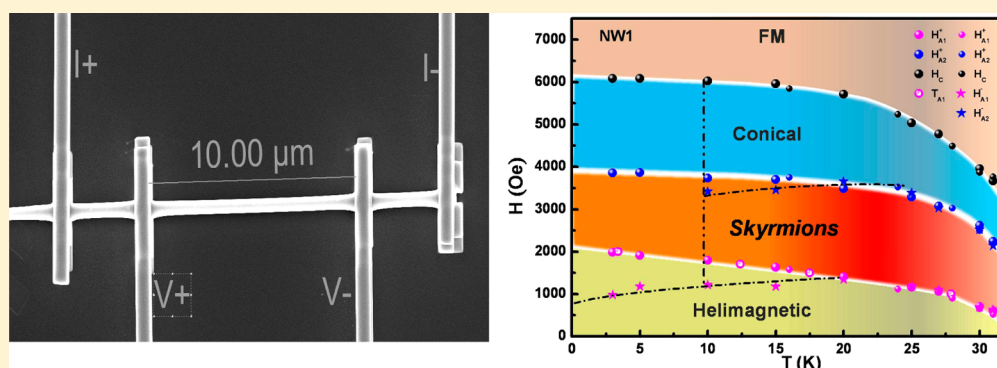
Haifeng Du,^{†,‡} John P. DeGrave,[§] Fei Xue,^{†,‡} Dong Liang,[§] Wei Ning,^{†,‡} Jiyong Yang,^{†,‡} Mingliang Tian,^{*,†,‡} Yuheng Zhang,^{†,‡} and Song Jin^{*,§}

[†]High Magnetic Field Laboratory, Chinese Academy of Science, Hefei 230031, Anhui, People's Republic of China

[‡]Hefei National Laboratory for Physical Science at The Microscale, University of Science and Technology of China (USTC), Hefei 230026, People's Republic of China

[§]Department of Chemistry, University of Wisconsin—Madison, 1101 University Avenue, Madison, Wisconsin 53706, United States

S Supporting Information



ABSTRACT: Topologically stable magnetic skyrmions realized in B20 metal silicide or germanide compounds with helimagnetic order are very promising for magnetic memory and logic devices. However, these applications are hindered because the skyrmions only survive in a small temperature-field (T – H) pocket near the critical temperature T_c in bulk materials. Here we demonstrate that the skyrmion state in helimagnetic MnSi nanowires with varied sizes from 400 to 250 nm can exist in a substantially extended T – H region. Magnetoresistance measurements under a moderate external magnetic field along the long axis of the nanowires ($H_{||}$) show transitions corresponding to the skyrmion state from $T_c \sim 32$ K down to at least 3 K, the lowest temperature in our measurement. When the field is applied perpendicular to the wire axis (H_{\perp}), the skyrmion state was not resolvable using the magnetoresistance measurements. Our analysis suggests that the shape-induced uniaxial anisotropy might be responsible for the stabilization of skyrmion state observed in nanowires.

KEYWORDS: Skyrmion, MnSi, nanowire, helimagnets, magnetotransport, spintronics

Over the last three decades, one-dimensional (1D) magnetic nanowires (NWs) have attracted much attention due to their unique magnetic properties as a result of the finite size effect as well as the potential applications in magnetic storage technologies.^{1–3} A representative example is the racetrack memory,⁴ where the ferromagnetic permalloy (Ni₈₁Fe₁₉) NW is encoded via control of magnetic domains using spin polarized current pulses. This design is expected to offer a denser, faster, and simpler storage technology that may replace current hard-disk drive. However, it generates large ohmic heating due to the high current density required to move the domain walls of ferromagnetic materials. More recently, a novel type of topologically stable vortex-like spin textures, called skyrmions,⁵ have been discovered in noncentrosymmetric B20 compounds with helical ground state, such as MnSi.⁶ One of its prominent features is that the threshold current density to move a skyrmion is on the order of 10⁶ A/m², which is much smaller than the current density required ($\sim 10^{12}$ A/m²) to move the domain walls in ferromagnetic

materials.^{7,8} This property makes skyrmions promising for applications in the racetrack memory with the advantage of negligible ohmic heating.

Within the theoretical framework of a phenomenological model for cubic helimagnets,^{9,10} spin arrangements occur as a consequence of couplings among several intrinsic interactions with different hierarchic energy scales including the strongest ferromagnetic exchange interaction, the intermediate Dzyaloshinskii–Moriya (DM) spin–orbit coupling originated from the lack of inversion symmetry in the crystal structure, as well as the weakest crystalline field energy. Generally, below the paramagnetic to helical transition temperature (T_c), a helimagnetic ground state is predicted due to the competition between ferromagnetic and DM couplings. When an external magnetic field is applied above a threshold value, the

Received: January 16, 2014

Revised: February 21, 2014

Published: March 14, 2014

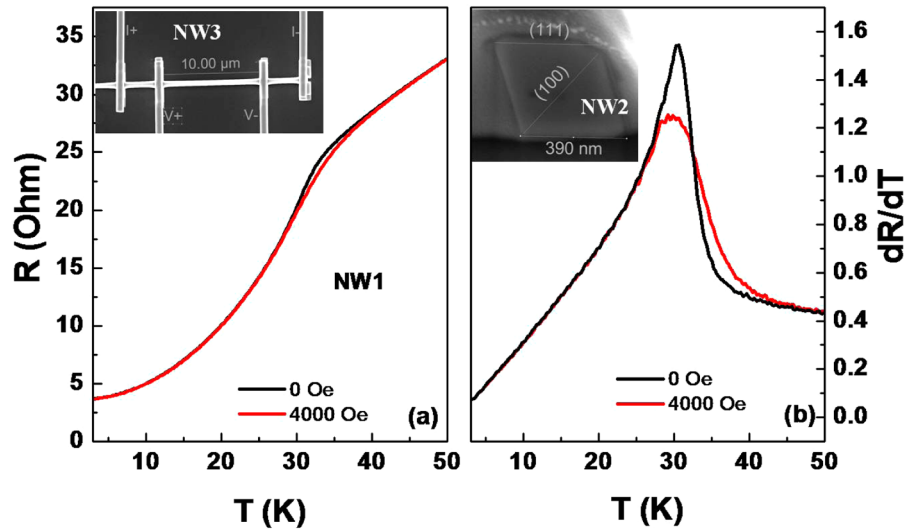


Figure 1. (a) Resistance R and (b) its derivative dR/dT as a function of temperatures (T) of NW1 at two typical magnetic fields (0 Oe, 4000 Oe) aligned parallel to the wire axis. The anomaly at $T_c \sim 32$ K represents the magnetic transition of the wire. Only one peak is observed around T_c in dR/dT curves at zero magnetic field, which is in contrast to the well-known dR/dT form in bulk MnSi at ambient pressure with a sharp peak followed by a shoulder around T_c . The inset in (a) shows a typical SEM image of the FIB-deposited four Pt electrode device on an individual MnSi nanowire. The inset in (b) shows the shape of the cross section of MnSi NW2, where the wire width is about 390 nm and the crystal orientations are also marked.

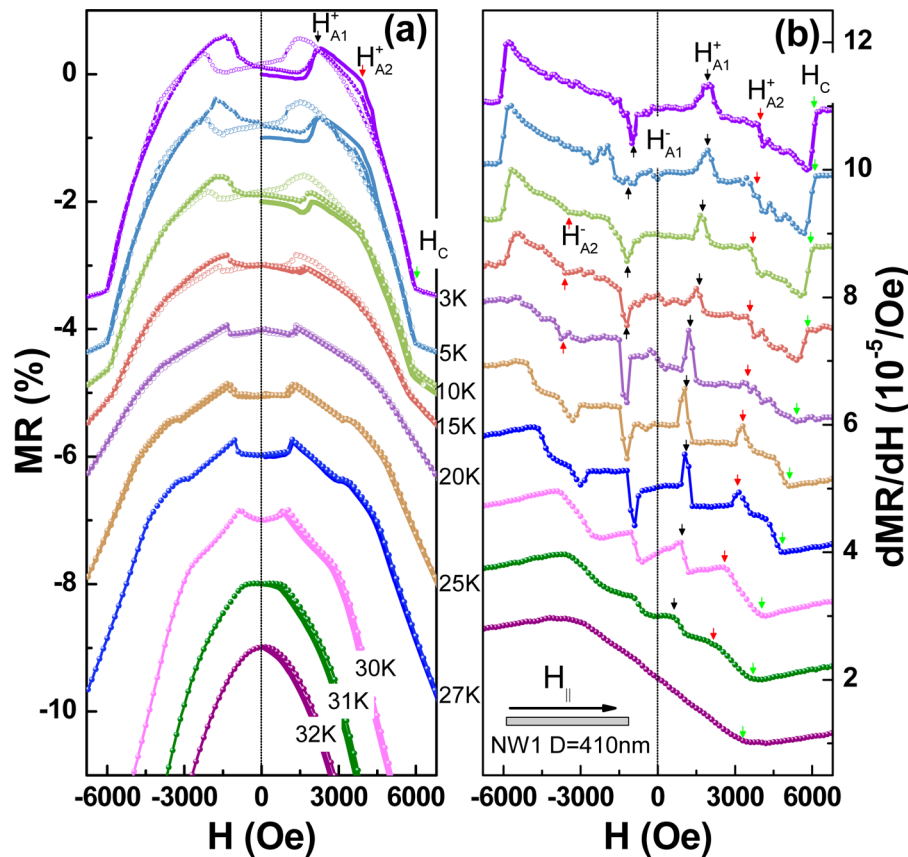


Figure 2. The magnetic field dependence of the MR and its derivative on external magnetic field for NW1. (a) Typical variation of the normalized MR as a function of external magnetic field $H_{||}$ at various temperatures. Starting at zero field, the upward curves are the initial MR curves (bold lines). The downward curves (open symbols) after saturation, along with the lower return curves (solid symbols), form the main loops. For $T < T_c$ with increasing $H_{||}$ from 0 Oe to 7000 Oe, helimagnetic, skyrmions, conical phase, and field-polarized ferromagnetic state (FM) appear in turn. Below 20 K, hysteresis effects are observed. (b) The derivative dMR/dH for the same data in (a) as a function of $H_{||}$ under the rising field cycle from which the transition fields H_{A1} and H_{A2} are defined and marked as arrows. The peak at H_{A1} indicates the first-order phase transition from helimagnetic to skyrmion states. Values for increasing and decreasing field strength are denoted by the superscripts “+” and “-”, respectively. H_c is defined from the kink as the transition from the conical phase to FM. Each curve is shifted vertically for clarity.

helimagnetic state transforms into a conical phase, and very close to the T_c , a new skyrmion phase emerges due to the stabilizing effect of thermal fluctuation. This fundamental model shows a close agreement with experimental observations^{6,9} but implies that the skyrmions only persist in a relatively narrow temperature-field (T – H) range near T_c in bulk materials, thus presenting a considerable obstacle to practical applications. Beyond bulk materials, both Lorentz transmission electron microscopy (LTEM) imaging^{11–13} and Hall effect measurements^{14,15} demonstrated that skyrmion state may be realized in an more extended T – H window when the dimensionality of helimagnets is lowered from bulk crystals to 2D films owing to the effect of spatial confinement effects¹⁶ or the uniaxial distortion.¹⁷ These findings naturally gave rise to an open question whether the skyrmion state is further stabilized in 1D system^{18–20} because skyrmions in 1D NWs are expected to have great potential for applications in spintronic nanodevices.^{5,21} Moreover, a recent LTEM study²² on a thin MnSi strip carved from a 400 nm MnSi NW using focused-ion beam (FIB) demonstrated the existence of skyrmion lattice in an more extended T – H regime, where the sample has a rectangular cross-section with a thickness of about 50 nm in order to reduce obstructive Fresnel fringes and facilitate LTEM observations.

Here, we present a magnetotransport study on single crystal MnSi NWs with size from 400 to 250 nm, and for the first time clearly revealed that the highly stable skyrmion state exists from the T_c of ~ 32 K down to 3 K (the lowest temperature possible in our experiment) in an external magnetic field aligned along the long axis of the NWs (H_{\parallel}) but was barely resolved in a perpendicular field (H_{\perp}) by the same probing technique. These data suggest that the enhanced stability of skyrmion state in MnSi NWs under H_{\parallel} is likely the consequence of the shape-induced uniaxial anisotropy.

All single crystal MnSi NWs used in this work were synthesized by a chemical vapor deposition method¹⁸ and they have a parallelogram cross-section (see the inset of Figure 1b). Four Pt electrodes, as shown in the inset of Figure 1a, were patterned on an individual wire using focused-ion beam (FIB) technique. Magnetoresistance (MR) measurements were carried out on three samples, named as NW1 (width ~ 410 nm), NW2 (~ 390 nm) and NW3 (~ 256 nm), respectively, by standard 4-probe techniques (The detailed device parameters are shown in Table S1 in the Supporting Information). The average room temperature resistivity of three samples is $\rho \approx 235 \pm 30 \mu\Omega\text{cm}$, which is quite close to the value of $220 \mu\Omega\text{cm}$ reported for bulk single-crystal MnSi,²³ indicating the excellent contact and high quality of the wires. The representative magnetotransport data discussed in the main text are mainly from NW1. Others are shown in the Supporting Information and the different wires show very similar features qualitatively.

The typical temperature dependence of the resistance R and its derivative on temperature dR/dT for NW1 at two different magnetic fields aligned parallel to the NW axis are shown in Figure 1a,b, respectively. The $dR/dT(T)$ data show only one λ -like peak around T_c (Figure 1b). These findings are in contrast with the well-known dR/dT form with a sharp peak followed by a shoulder around T_c in bulk MnSi at ambient pressure but show close agreement with the observations of MnSi crystal at high pressure.²³ The T_c of NW1 is determined to be ~ 32 K from the $MR(T)$ data discussed later, which is ~ 2.5 K higher than that of bulk MnSi (29.5 K). The enhanced T_c in MnSi is generally suggested to be due to the lattice strain and the

increase of the crystal lattice spacing, as discussed in MnSi(111) films¹⁵ and Ge-doped MnSi crystals²⁴ owing to the heteroepitaxial tensile strain and chemical-induced negative pressure, respectively. Similarly, we suggest that the lattice strain probably plays a similar role in the MnSi NWs due to the nanoscale morphology.

We now turn to the detailed behavior of the MR – H isotherms in the low magnetic fields below T_c . Figure 2a shows the $MR = [R(H) - R(0)]/R(0)$ of NW1 as a function of H_{\parallel} at various temperatures. Importantly, a hysteresis loop emerges in the MR data below 20 K. Such hysteresis phenomenon in MR – H curves has been observed in bulk MnSi single crystals under high pressure²⁵ but disappears at ambient pressure.^{26,27} Meanwhile, this hysteresis indicates that the magnetic states in MnSi NWs are sensitive to the temperature and field history. In light of the importance of temperature and field history, for each measurement we cooled the NWs to the defined temperature from far above T_c (e.g., ~ 50 K) in zero magnetic field before recording the MR data. As shown in Figure 2a, the upward curves starting at the zero fields in each panel are the initial MR curves (bold lines), which reflect the properties of MnSi NWs under zero field cooling (ZFC). The sweeping down curves (open symbols) from the saturation fields, along with the sweeping up curves (solid symbols) from below, recorded the full loops. These loops correspond to the properties under the field cooling (FC). It is noted that above 10 K, there is no obvious difference between the curves under FC and ZFC. However, below 10 K the MR curves after ZFC show more significant features that are closely related to the magnetic phase transitions than those after FC. But, this difference does not severely affect the recognition of the transition fields as defined below.

Next, we show the important field-driven evolution of chiral spin textures in the MnSi NW. Above $T_c \sim 32$ K, the MR is negative and without any specific features (see Figure S1 in Supporting Information), which is consistent with the typical results reported in various MnSi samples including 3D bulk,²⁸ 2D films,¹⁵ as well as 1D NWs.¹⁸ At temperatures below T_c , starting from $H_{\parallel} = 0$ Oe to 7000 Oe, besides the kink at saturation field H_c , two anomalous kinks, as indicated by H_{A1} and H_{A2} in Figure 2a, sequentially appear.

These anomalies clearly survive from T_c down to 3 K (the lowest temperature in our experiment). Previous works on both pure²⁸ and Fe-doped MnSi²⁹ bulk single-crystals have established that these two kinks in the MR – H isotherms correspond to the lower and upper critical fields driving the system into and out the so-called A phase,²⁸ which has by now been identified as the skyrmion state by means of small-angle neutron scattering (SANS)⁶ and other measurements.²⁶ Moreover, the skyrmion phase boundaries in Fe-doped MnSi single-crystals obtained by the MR measurements agree well with those by topological Hall effect measurements.²⁹ Meanwhile, the dependence of the initial MR curves (H_{\parallel} from 0 Oe to 7000 Oe) on temperature are highly consistent with the MR – H isotherms of bulk MnSi single crystals under pressure, where a larger topological Hall effect is simultaneously observed.³⁰ These similar features in M – H curves between MnSi bulk and NWs provide clear proof that the skyrmion state not only exists in this 1D NW under an excitation of a moderate H_{\parallel} but also becomes more stabilized in an extended T – H range.

To better survey the field-driven evolution of the chiral spin textures in MnSi NWs, in Figure 2b we examine more closely

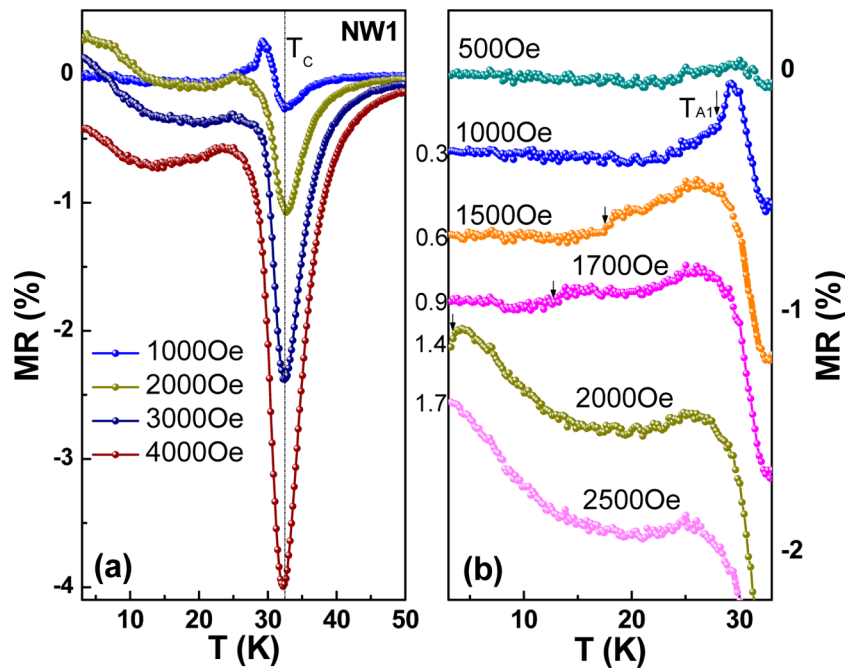


Figure 3. Temperature dependence of the MR for NW1. (a) The overall dependence of MR on T under various parallel magnetic fields; a minimum is shown as the T_c due to the suppression of carrier scattering from spin fluctuations. More pronounced behavior below T_c under low magnetic fields is highlighted in panel (b). A complex temperature dependence with a pronounced top-hat-shaped peak is seen between the temperature range T_c and T_{A1} . The width of the peak increases with the increasing H up to 2000 Oe. These data demonstrated that skyrmions exist below T_{A1} . For clarity, the curves are shifted downward with offset value marked on the left.

the derivative dMR/dH in the upward sweeping cycle of the magnetic field for the same data displayed in Figure 2a, from which, we defined the transition fields H_{A1} , H_{A2} , and H_c , as marked by the arrows. Values for positive and negative magnetic fields are denoted by the superscripts “+” and “−”, respectively. The helimagnetic phase is realized below the lower critical field H_{A1} . With the increase of magnetic field, the helimagnetic phase transforms into the skyrmion state via a first order phase transition, manifested as very sharp peaks at H_{A1} due to the completely different topological properties between helimagnetic and skyrmion state.⁶ Above the upper critical field H_{A2} , the system transforms into the conical phase from skyrmion state. However, the theoretically predicted first order transition⁹ at H_{A2} is less visible at temperatures of $T < 15$ K with the broadened transition boundary. Such a broadening might be a consequence of the possible coexistence of the skyrmion states and the conical phases near the first-order boundary in a small parameter range, as suggested in high quality single crystal MnSi by magnetization and susceptibility measurements.²⁶ Beyond the field H_c at the shoulder in Figure 2a (or the kink in Figure 2b), the system finally transitions into the field polarized ferromagnetic state (FM). These results corroborate the well-established scenario in cubic helimagnets that helimagnetic phase, skyrmion state and conical phase appear in turn with the increase of the external magnetic field.⁹

The significantly extended T – H region for skyrmion state is further confirmed by the temperature dependent MR measurements at different $H_{||}$. All $MR(T)$ data were recorded on increasing temperature scan under zero-field cooling to avoid metastable phase. Figure 3a shows the overall MR of NW1, as a function of T under various magnetic fields, where a deep valley is shown at T_c due to the suppression of carrier scattering from the spin fluctuations by $H_{||}$.²⁸ Below T_c at $H_{||} < 2500$ Oe, more complex behavior that sensitively varies with the increase of $H_{||}$

is seen and plotted in Figure 3b (the enlarged part of Figure 3a), where a pronounced top-hat-shaped peak appears between T_c and T_{A1} . The width of the peak $\Delta T = T_c - T_{A1}$ increases with the increasing $H_{||}$ up to 2000 Oe. A comparative analysis of the MR versus T and MR versus H data allows us to conclude that T_{A1} corresponds to the lower critical temperature of the skyrmion state.

Combining these magnetotransport data in $R(H_{||})$ and $R(T)$, a magnetic phase diagram for NW1 was constructed as shown in Figure 4 in which the solid symbols are defined from H_{A1} , H_{A2} , and H_c in $R(H_{||})$ curves and the open symbols are defined from T_{A1} in the $R(T)$ curves. The skyrmion state is clearly stabilized over a broad region in the T – H plane, spanning from the T_c down to 3 K under ZFC, and occupying almost one-third of the regions below H_c . This experimental observation of magnetic states is in contrast to the magnetic phase diagrams of previous reported MnSi samples with various morphologies and dimensionalities (reproduced as Figure S2 in the Supporting Information). In bulk single-crystal MnSi, the skyrmion phase can only exist as a metastable state in a small T – H plane from about 26 to 28.5 K and 1000 to 2500 Oe embedded in the conical phase region.^{6,26} In MnSi film thinned from the bulk, the skyrmion phase is stable from T_c of about 22 K down to the lowest measured temperature 6 K.¹³ However, the external field is applied perpendicular to plane and no conical phase appears in the magnetic phase due to the spatial confinement effect.¹⁶

As the metastable behavior emerges under FC below 20 K, the dotted lines shown in Figure 4 are the phase boundaries for decreasing fields from above. Both the critical fields H_{A1} and H_{A2} under FC clearly deviate from the phase boundaries under ZFC, and when $T < 10$ K, the phase boundary at H_{A2} is no longer resolved, indicating the possible coexistence of the skyrmion state and conical phase. In addition to the MR measurements under $H_{||}$, we have also performed the MR

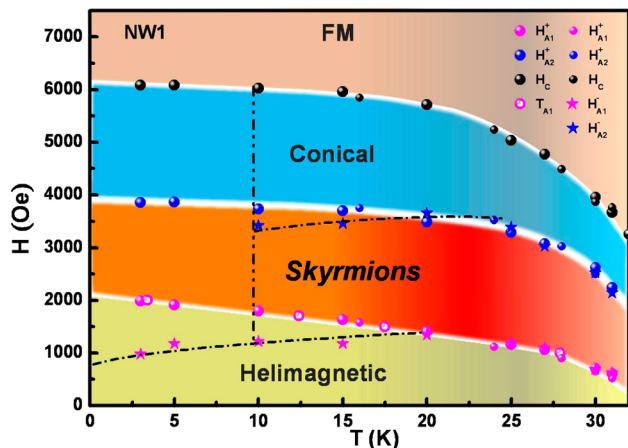


Figure 4. Magnetic phase diagram of NW1 under parallel magnetic field H_{\parallel} inferred from MR data. Solid and open symbols represent data obtained from $R(H)$ and $R(T)$, respectively. Small circles represent the data from $R(H)$ under small measured currents. Solid stars denote the data from $R(H)$ for decreasing field strength. Skyrmions survive in a large T – H window down to the lowest temperature possible in the measurement (3 K) for increasing field strength. For decreasing field strength, the critical fields H_{A1} and H_{A2} appear to decrease slightly below 20 K. Below 10 K, no obvious phase boundaries exist between skyrmion state and conical phase.

measurements in an external field H_{\perp} aligned perpendicular to the wire axis (Figure 5), where both $R(H_{\perp})$ and $R(T)$ curves show smooth variations without any specific anomalies corresponding to the skyrmion phase as seen under parallel H_{\parallel} . This observation seems to intuitively imply the lack of skyrmion states under H_{\perp} , which is in contrast to the recent LTEM study on MnSi NW under H_{\perp} condition, where the extended skyrmion state was observed down to 6 K (see Figure S2 in the Supporting Information).²² Such a difference between MR data and LTEM data could be a consequence of the geometrical difference of the MnSi samples. The MnSi NW observed in LTEM was thinned to 50 nm by FIB in order to reduce obstructive Fresnel fringes and facilitate TEM observations. Therefore, the LTEM results could be explained within

the framework of the spatial confinement for a nanometer-sized thin film,¹⁹ which is in contrast to our current experimental geometry with a high aspect ratio NW of several hundred nanometers diameter. There are also other factors that might cause the apparent invisibility of the skyrmion phase by MR measurements under H_{\perp} . For instance, the NW orientation and shape make its magnetic hard axis perpendicular to the wire axis. The increasing demagnetizing field makes the signatures at the transition less pronounced, as reported in bulk MnSi with different shape by magnetization and susceptibility measurements.²⁶ Meanwhile, the magnetization and susceptibility data indicate that the signatures of A (skyrmion) phase depend on the crystallographic orientation, where the signatures are most pronounced for the $\langle 100 \rangle$ axis, while they are weakest for the $\langle 111 \rangle$ axis.²⁶ Under transverse MR configurations, the external field is actually along the $\langle 111 \rangle$ crystallographic axis for the rhombohedral cross-section of B20 silicide NW,³¹ as shown in the inset of Figure 1b. This crystal orientation might also weaken the MR signatures of skyrmion phase in the transport measurements. Therefore, the magnetic phase diagram of MnSi NWs under H_{\perp} remains inconclusive using MR measurements and other experimental methods such as Hall effect measurements³² may be more effective to clarify the situation.

In order to elucidate the mechanism for the formation of the highly stable skyrmion state in MnSi NWs under H_{\parallel} , we briefly summarize the existing experiments and theories to stabilize the skyrmion state. Highly stable skyrmion state has been observed in 2D MnSi materials.^{13,15} Three mechanisms were proposed to explain the extended skyrmion state. The first is based on the spatial confinement effects.¹⁶ When the thickness of the film is below a threshold, a type of 3D Skyrmions, characterized by a superposition of conical modulations along the Skyrmion axis and double-twist rotation in the perpendicular plane, is thermodynamically stable in a broad T – H range with H normal to the film plane. This mechanism may explain the experimental results in 2D MnSi materials including mechanically thinned flakes and homogeneous films,^{11–15} even quasi-2D MnSi nanostripes.²³ But this mechanism makes sense only if the film thickness is comparable to or less than the skyrmion lattice constant L_D , which is therefore not suitable for the

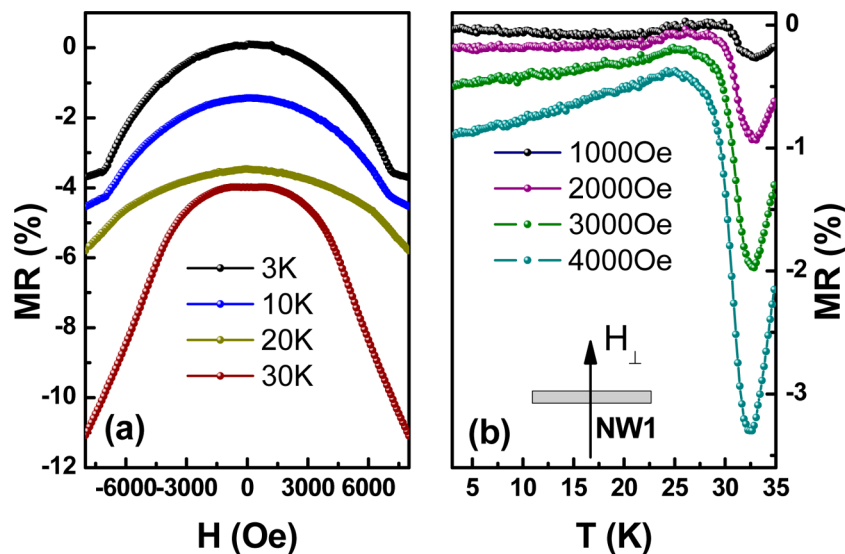


Figure 5. The magnetic field (a) and temperature (b) dependence of the MR for NW1 under perpendicular fields H_{\perp} . Both $R(H_{\perp})$ and $R(T)$ curves show smooth variation and no obvious phase boundaries are observed to identify skyrmion states. For clarity, the curves in (a) are shifted.

present system since the length and thickness of NWs are much larger than the $L_D = 18$ nm for MnSi. The second mechanism invokes the uniaxial anisotropy originating from the surface, interface, or pressure.¹⁷ When applying the external magnetic field along the easy axis, the combination of the uniaxial anisotropy and the external magnetic field leads to the significant increase of conical phase energy and thus stabilizes the skyrmion state. The last mechanism³³ also involves uniaxial anisotropy, but with its hard axis perpendicular to the film plane. Extended elliptical skyrmion gratings or discrete helical states³⁴ are suggested as a thermodynamically stable state when applying the external magnetic field in the film plane. Actually, the last two mechanisms can be unified in one argument that an effective uniaxial anisotropy may stabilize skyrmion state if the magnetic field is applied parallel to the easy axis of the effective uniaxial anisotropy. This is indeed the case in the MnSi NWs under H_{\parallel} , where the magnetostatic interaction would generate an effective uniaxial anisotropy with its easy axis along the NW axis. Quantitatively, the effective field H_u of shape-induced uniaxial anisotropy, extracted from the difference of the saturation field H_c between transverse and longitudinal configurations, is determined to be ~ 900 Oe at low temperature. Here, we leave the magnetocrystal anisotropy out of consideration because it is very weak, as verified by earlier ferromagnetic resonance experiment.³⁵ As a result, the critical parameter H_u/H_c that determines the stability of skyrmion phase is ~ 0.15 , which is well within the region for stable skyrmion states according to the theoretical calculation.¹⁶

In conclusion, magneto-transport experiments show that skyrmion states are stable over a significantly larger T – H range in MnSi nanowires under parallel magnetic field while the magnetic phase diagram of intact MnSi NWs under H_{\perp} remains inconclusive using MR measurements. The mechanism to stabilize the skyrmions in parallel H_{\parallel} is most likely the effect of shape-induced uniaxial anisotropy. These findings are of great importance not only for fundamental understanding of skyrmion physics in reduced dimensions but also for future high density magnetic storage technology where stable skyrmions in 1D magnetic system could be manipulated with ultralow spin-polarized current density.

■ ASSOCIATED CONTENT

■ Supporting Information

Detailed methods and supplemental figures for nanowires NW1, NW2, and NW3. This material is available free of charge via the Internet at <http://pubs.acs.org>.

■ AUTHOR INFORMATION

Corresponding Authors

*E-mail: tianml@hmf.ac.cn.

*E-mail: jin@chem.wisc.edu.

Author Contributions

S.J., M.T., and Y.Z. supervised the research. J.P.D. and D.L. synthesized the MnSi nanowires. H.D. and F.X. fabricated the devices. H.D., J.Y., and W.N. carried out the transport measurements in PPMS. H.D., M.T., J.P.D., D.L., and S.J. contributed to the analysis. H.D., J.P.D., D.L., M.T., and S.J. wrote the paper, together with help of all other coauthors.

Notes

The authors declare no competing financial interest.

■ ACKNOWLEDGMENTS

This work was supported by the National Key Basic Research of China, under Grants 2011CBA00111 and 2010CB923403; the National Nature Science Foundation of China, Grants 11174294, 11374302, 11104281, and 11104280, and U.S. National Science Foundation, Grant ECC-1231916. Dr. Tian also thanks the support of the Hundred Talents Program of the Chinese Academy of Science. The authors thank Weike Wang and Yuyan Han for the assistance in sample measurements by PPMS, and Professor. Martino Poggio for providing nanowire transferring facilities.

■ REFERENCES

- (1) Sellmyer, D. J.; Zhang, M.; Skomski, R. *J. Phys.: Condens. Matter.* **2001**, *13*, R433–R460.
- (2) Vernier, N.; Allwood, D. A.; Atkinson, D.; Cooke, M. D.; Cowburn, R. P. *Europhys. Lett.* **2004**, *65*, 526–532.
- (3) Brataas, A.; Kent, A. D.; Ohno, H. *Nat. Mater.* **2012**, *11*, 372–381 and reference therein..
- (4) Parkin, S. S. P.; Hayashi, M.; Thomas, L. *Science* **2008**, *320*, 190–194.
- (5) Nagaosa, N.; Tokura, Y. *Nat. Nanotechnol.* **2013**, *8*, 899–911.
- (6) Mühlbauer, S.; Binz, B.; Jonietz, F.; Pfleiderer, C.; Rosch, A.; Neubauer, A.; Georgii, R.; Böni, P. *Science* **2009**, *323*, 915–919.
- (7) Jonietz, F.; Mühlbauer, S.; Pfleiderer, C.; Münzer, W.; Bauer, A.; Adams, T.; Georgii, R.; Boni, P.; Duine, R. A.; Everschor, K.; Garst, M.; Rosch, A. *Science* **2010**, *330*, 1648–1651.
- (8) Yu, X. Z.; Kanazawa, N.; Zhang, W. Z.; Nagai, T.; Hara, T.; Kimoto, K.; Matsui, Y.; Onose, Y.; Tokura, Y. *Nat. Commun.* **2012**, *3*, 988.
- (9) Rößler, U. K.; Leonov, A. A.; Bogdanov, A. N. *J. Phys.: Conf. Ser.* **2011**, *303*, 012105/1–012105/12.
- (10) Rößler, U. K.; Bogdanov, A. N.; Pfleiderer, C. *Nature* **2006**, *442*, 797–801.
- (11) Yu, X. Z.; Onose, Y.; Kanazawa, N.; Park, J. H.; Han, J. H.; Matsui, Y.; Nagaosa, N.; Tokura, Y. *Nature* **2010**, *465*, 901–904.
- (12) Yu, X. Z.; Kanazawa, N.; Onose, Y.; Kimoto, K.; Zhang, W. Z.; Ishiwata, S.; Matsui, Y.; Tokura, Y. *Nat. Mater.* **2011**, *10*, 106–109.
- (13) Tonomura, A.; Yu, X. Z.; Yanagisawa, K.; Matsuda, T.; Onose, Y.; Kanazawa, N.; Park, H. S.; Tokura, Y. *Nano Lett.* **2012**, *12*, 1673–1677.
- (14) Huang, S. X.; Chien, C. L. *Phys. Rev. Lett.* **2012**, *108*, 267201/1–267201/5.
- (15) Li, Y. F.; Kanazawa, N.; Yu, X. Z.; Tsukazaki, A.; Kawasaki, M.; Ichikawa, M.; Jin, X. F.; Kagawa, F.; Tokura, Y. *Phys. Rev. Lett.* **2013**, *110*, 117202/1–117202/5.
- (16) Rybakov, F. N.; Borisov, A. B.; Bogdanov, A. N. *Phys. Rev. B* **2013**, *87*, 094424/1–094424/4.
- (17) Butenko, A. B.; Leonov, A. A.; Rossler, U. K.; Bogdanov, A. N. *Phys. Rev. B* **2010**, *82*, 052403/1–052403/4.
- (18) Higgins, J. M.; Ding, R.; DeGrave, J. P.; Jin, S. *Nano Lett.* **2010**, *10*, 1605–1610.
- (19) Seo, K.; Yoon, H.; Ryu, S.-W.; Lee, S.; Jo, Y.; Jung, M.-H.; Kim, J.; Choi, Y.-K.; Kim, B. *ACS Nano* **2010**, *4*, 2569–2576.
- (20) DeGrave, J. P.; Schmitt, A. L.; Selinsky, R. S.; Higgins, J. M.; Keavney, D. J.; Jin, S. *Nano Lett.* **2011**, *11*, 4431–4437.
- (21) Fert, A.; Cros, V.; Sampaio, J. *Nat. Nanotechnol.* **2013**, *8*, 152–156.
- (22) Yu, X. Z.; DeGrave, J. P.; Hara, Y.; Hara, T.; Jin, S.; Tokura, Y. *Nano Lett.* **2013**, *13*, 3755–3759.
- (23) Petrova, A. E.; Stishov, S. M. *Phys. Rev. B* **2012**, *86*, 174407/1–174407/15.
- (24) Potapova, N.; Dyadkin, V.; Moskvina, E.; Eckerlebe, H.; Menzel, D.; Grigoriev, S. *Phys. Rev. B* **2012**, *86*, 060406/1–060406/4.
- (25) Ritz, R.; Halder, M.; Franz, C.; Bauer, A.; Wagner, M.; Bamler, R.; Rosch, A.; Pfleiderer, C. *Phys. Rev. B* **2013**, *87*, 134424/1–134424/17.

- (26) Bauer, A.; Pfeleiderer, C. *Phys. Rev. B* **2012**, *85*, 214418/1–214418/16.
- (27) Lee, M.; Onose, Y.; Tokura, Y.; Ong, N. P. *Phys. Rev. B* **2007**, *75*, 172403/1–172403/4.
- (28) Kadowaki, K.; Okuda, K.; Date, M. *J. Phys. Soc. Jpn.* **1982**, *51*, 2433–2438.
- (29) Chapman, B. J.; Grossnickle, M. G.; Wolf, T.; Lee, M. *Phys. Rev. B* **2013**, *88*, 214406/1–214406/5.
- (30) Lee, M.; Kang, W.; Onose, Y.; Tokura, Y.; Ong, N. P. *Phys. Rev. Lett.* **2009**, *102*, 186601–4.
- (31) Szczech, J. R.; Schmitt, A. L.; Bierman, M. J.; Jin, S. *Chem. Mater.* **2007**, *19*, 3238–3243.
- (32) DeGrave, J. P.; Liang, D.; Jin, S. *Nano Lett.* **2013**, *13*, 2704–2709.
- (33) Wilson, M. N.; Karhu, E. A.; Quigley, A. S.; Rossler, U. K.; Butenko, A. B.; Bogdanov, A. N.; Robertson, M. D.; Monchesky, T. L. *Phys. Rev. B* **2012**, *86*, 144420/1–144420/6.
- (34) Wilson, M. N.; Karhu, E. A.; Lake, D. P.; Quigley, A. S.; Meynell, S.; Bogdanov, A. N.; Fritzsche, H.; Rößler, U. K.; Monchesky, T. L. *Phys. Rev. B* **2013**, *88*, 214420/1–214420/6.
- (35) Date, M.; Okuda, K.; Kadowaki, K. *J. Phys. Soc. Jpn.* **1977**, *42*, 1555–1561.